

Arbitrary-order exceptional points in a nanomechanical cavity

Authors: Ning Wu^{1,2}, Kaiyu Cui^{1,2,*}, Ziming Chen^{1,2}, Chenxuan Wang^{1,2}, Xue Feng^{1,2}, Fang Liu^{1,2}, Wei Zhang^{1,2,3}, Hao Sun^{1,2}, Yongzhuo Li^{1,2}, and Yidong Huang^{1,2,3,*}

Affiliations:

¹ Department of Electronic Engineering, Tsinghua University, Beijing 100084, China

² Beijing National Research Center for Information Science and Technology (BNRist), Tsinghua University, Beijing 100084, China

³ Beijing Academy of Quantum Information Sciences, Beijing, China

*Corresponding author: kaiyucui@tsinghua.edu.cn; yidonghuang@tsinghua.edu.cn

Abstract: Higher-order exceptional points (EPs) govern non-Hermitian system dynamics through their enriched and sharpened spectral topology, yet the intrinsic topological fragility hinders robust experimental realization. Here, we present a scalable architecture that implements arbitrary-order EPs via a recurrent network comprising a single nanomechanical resonator and unlimited virtual resonators. We experimentally realize mechanical EPs up to the seventh order and confirm this architecture's scalability. Moreover, we reveal that the fundamental noise component and the measured signal share the same system coupling channel and thus undergo identical root-response amplification near EPs of arbitrary order, consistent with our signal-to-noise ratio measurements. Our work establishes a general platform for exploring higher-order EP-based phenomena while clarifying the fundamental boundary of non-Hermitian sensitivity enhancement across diverse physical systems.

Non-Hermitian physics describes the dynamics of open systems that exchange energy with the environment, encompassing phenomena across multiple scales from particle decay (1), decoherence of photons and phonons (2), and collective dynamics of active matter (3) to black hole evolution (4). In such non-Hermitian systems, exceptional points (EPs) emerge as nontrivial spectral singularities, where the eigenvalues and eigenvectors coalesce simultaneously (5–9). Unlike Hermitian degeneracies, the EPs exhibit a Riemann-surface topology and an associated phase transition. These features not only result in peculiar dynamical behavior but also provide opportunities for developing highly sensitive sensors (10–12) and diverse mode-control devices (13–16). Early EP research primarily focused on second-order EPs, the simplest form of exceptional degeneracy. Extending the research to higher-order EPs shows the potential to explore richer topological phenomena in high-dimensional systems (5) and enhance sensor performance near EPs (17). For EP-based sensors, device performance is believed to be improved because the unique mode splitting scales with $\varepsilon^{1/N}$ near EPs. As the order N of EPs increases, the system exhibits a sharper spectral response to the perturbation ε .

Motivated by these potential advantages, numerous theoretical models (18–20) have been proposed to realize higher-order EPs. In parallel, third-order EPs have been demonstrated in a variety of physical platforms, including optical (17), optomechanical (21), spin (22), superconducting (23), and electrical (19, 24) systems. These implementations typically rely on cascading multiple physical modes. As the system dimensionality increases, additional coupling pathways for fundamental noise (quantum and thermal noise) are introduced, and the control of system parameters becomes increasingly demanding. These obstacles, together with the fragile topology near higher-order EPs, constrain the scalability of such EPs, making their practical realization a significant challenge. More crucially, although the sharper spectral response near higher-order EPs is well established and has been experimentally confirmed (17), whether a sensor’s fundamental sensitivity can be enhanced near EPs is currently under debate (11, 12, 24–30), mainly due to the previously overlooked dynamics of fundamental noise. To date, the advantages of higher-order EPs for sensing applications remain elusive.

In this study, we propose a universal architecture for realizing arbitrary-order EPs through a recurrent network consisting of a physical resonator and unlimited virtual resonators emulated via digital computation. Using this architecture, we experimentally demonstrate nanomechanical EPs

across multiple orders in both the linear and nonlinear (phonon-lasing) regimes by frequency topology mapping, including the realization of a seventh-order nonlinear EP (NEP). We further reveal that the fundamental noise component shares the same system coupling channel with the measured signal, resulting in the root-response co-amplification of both. This co-amplification mechanism prevents the fundamental sensitivity enhancement near EPs regardless of their order. Consistently, no improvement in signal-to-noise ratio (SNR) is observed experimentally near third- and seventh-order NEPs. Nevertheless, higher-order EPs still provide sensing advantages in systems dominated by specific forms of technical noise, particularly when such noise is decoupled from EP dynamics. This work establishes a scalable and versatile platform for arbitrary-order EPs and clarifies ongoing debates concerning fundamental sensitivity enhancement in non-Hermitian sensing. Our approach is transferable to diverse physical platforms, including spin (22), superconducting (23), and thermal (31) systems, paving the way for broader exploration of non-Hermitian topology and high-precision sensing with AI-based networks.

Results

The physical model for realizing arbitrary-order EPs is shown in Fig. 1A. The resonator mode b_0 is coupled to a set of modes $\{b_1, \dots, b_n\}$. The complex coefficients $J_j e^{i\phi_j/2}$ represent the coupling strength between b_0 and other modes b_j ($j=1, \dots, n$). If the complex frequencies $\Omega_j - i\gamma_j/2$ ($j=0 \dots n$) are set in advance, $J_j e^{i\phi_j/2}$ can be precisely calculated by solving inhomogeneous linear equations to realize the EPs (section S1). Conventionally, the direct way to construct such a higher-order EP is to couple multiple resonators in a real system. However, locating the singularity point within Riemann-surface topology becomes increasingly challenging as the dimensionality of the parameter space grows. Meanwhile, higher-order EPs are topologically fragile and exhibit extreme spectral sensitivity not only to the target signal but also to noise perturbations. Moreover, as the mode dimensionality increases, additional fundamental noise-coupling pathways are introduced into such systems, ultimately limiting the practical implementation and applications of higher-order EPs (6, 32, 33).

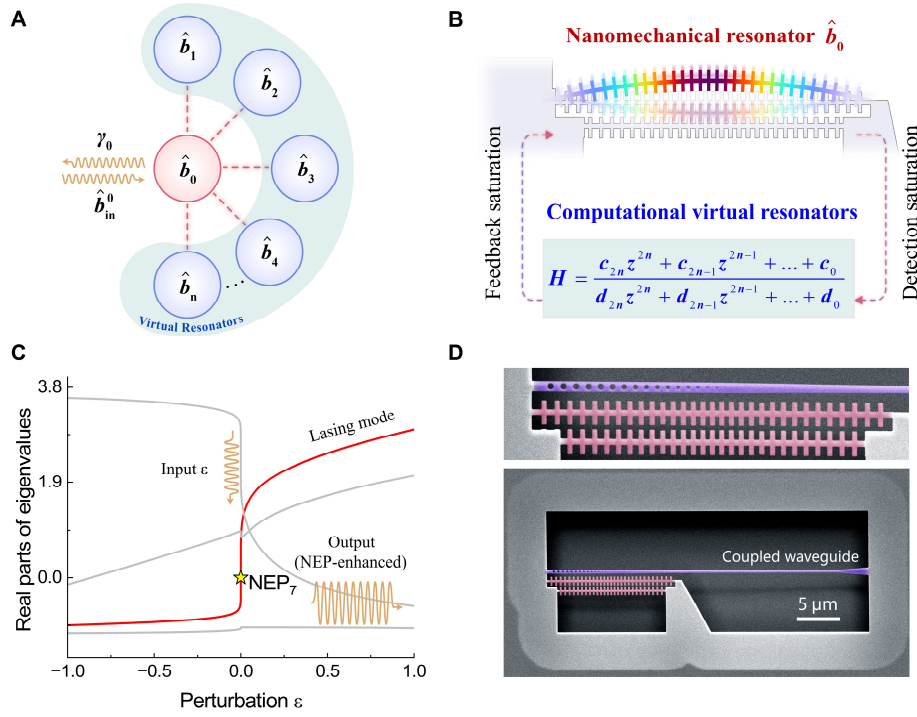


Fig. 1 The proposed physical model and its realization platform. (A) Physical model for realizing arbitrary-order EPs. b_0 is a real resonator that interacts with computationally defined virtual resonators b_1 to b_n . The coupling strength between b_0 and b_j is $J_j e^{i\phi_j/2}$. The mode b_0 loses energy to the thermal bath at rate γ_0 . (B) Physical platform for realizing arbitrary-order EPs. In this recurrent network, the nanomechanical resonator is coupled to an FPGA module, which emulates the virtual resonators. Feedback nonlinearity, arising from detection or output saturation, is used to realize NEPs. (C) Evolution of the real parts of eigenvalues near NEP_7 with a perturbation ε applied to the frequency of the real resonator. Red and gray curves represent the lasing mode and other thermal modes, respectively. (D) Scanning electron microscope (SEM) image of the fabricated silicon optomechanical cavity. The red and purple regions represent the fishbone cavity structure and the coupled waveguide, respectively.

To overcome these obstacles, we implement a hybrid physical–digital architecture based on a recurrent network that supports EPs of arbitrary order, as shown in Fig. 1B. By leveraging the formal equivalence between computational processes and physical evolution, we reduce the physical realization to a single real resonator b_0 for sensing, while emulating all other resonators b_j ($j=1, \dots, n$) and the interaction between b_0 and b_j through digital computation. Experimentally, the silicon optomechanical fishbone cavity acts as the real resonator b_0 , and an FPGA performs digital computation for feedback. The introduced digital computational process is immune to environmental perturbations, distinct from the analog implementation or the physical evolution

process. Meanwhile, the thermal and quantum fluctuations, which scale with the number of physical resonators, are absent from the ideal computational process. Although the additional optical shot noise in the measurement process sets the displacement readout imprecision and induces radiation-pressure backaction on the mechanical mode (34, 35), measurement noise at the order of mechanical zero-point motion is achievable (34–37). In this study, the measurement noise and other technical contributions remain negligible compared with the thermal noise acting on the single real resonator b_0 . Consequently, the challenges for realizing higher-order EPs are circumvented.

Furthermore, the system in Fig. 1B can enter the phonon lasing regime by increasing the coupling strength $J_j e^{i\phi_j/2}$. In this regime, the feedback saturation persists until the mode with the highest gain reaches the gain-loss balance point (33, 38). As a result, the NEPs (24, 26, 28, 39) can be realized by feedback saturation together with appropriately chosen system parameters. We propose a general method for realizing arbitrary-order NEPs through feedback saturation. Specifically, we predefine the system eigenvalues at NEPs of arbitrary order and solve inhomogeneous linear equations to obtain the corresponding complex frequencies $\Omega_j - i\gamma_j/2$ and coupling strengths $J_j^{NEP} e^{i\phi_j/2}$ (section S1). Accordingly, the FPGA coefficients are determined. Notably, the system eigenvalues at NEPs are not necessarily degenerate as in linear EPs (LEPs). This distinction arises because the system response of NEPs is not only determined by the instantaneous Hamiltonian (24) but also by the temporal dynamics of the system, which are controlled by the feedback saturation. When the perturbation ε induces changes in the nanobeam's frequency or linewidth, the eigenfrequency shift depends not only on ε but also on the relative feedback strength ζ . In the steady state, the coupling strength satisfies $J_j e^{i\phi_j/2} = J_j^{NEP} e^{i\phi_j/2} \sqrt{\zeta}$, and ζ is unity at NEPs. Moreover, because ζ depends nonlinearly on ε , the order of NEPs can exceed the number of resonators. For $n+1$ resonators, NEPs up to the $(2n)$ -th order, denoted as NEP_{2n} , can be achieved. As the even-order NEPs are semi-stable for the perturbation ε (section S1), we focus on the odd-order NEPs in this work. Fig. 1C displays the numerically calculated eigenvalue spectrum of a five-dimensional system, showing the non-degenerate eigenvalues at NEP_7 . The lasing frequency shift in the vicinity of NEP_7 scales with $\sqrt[3]{\varepsilon}$ (section S2).

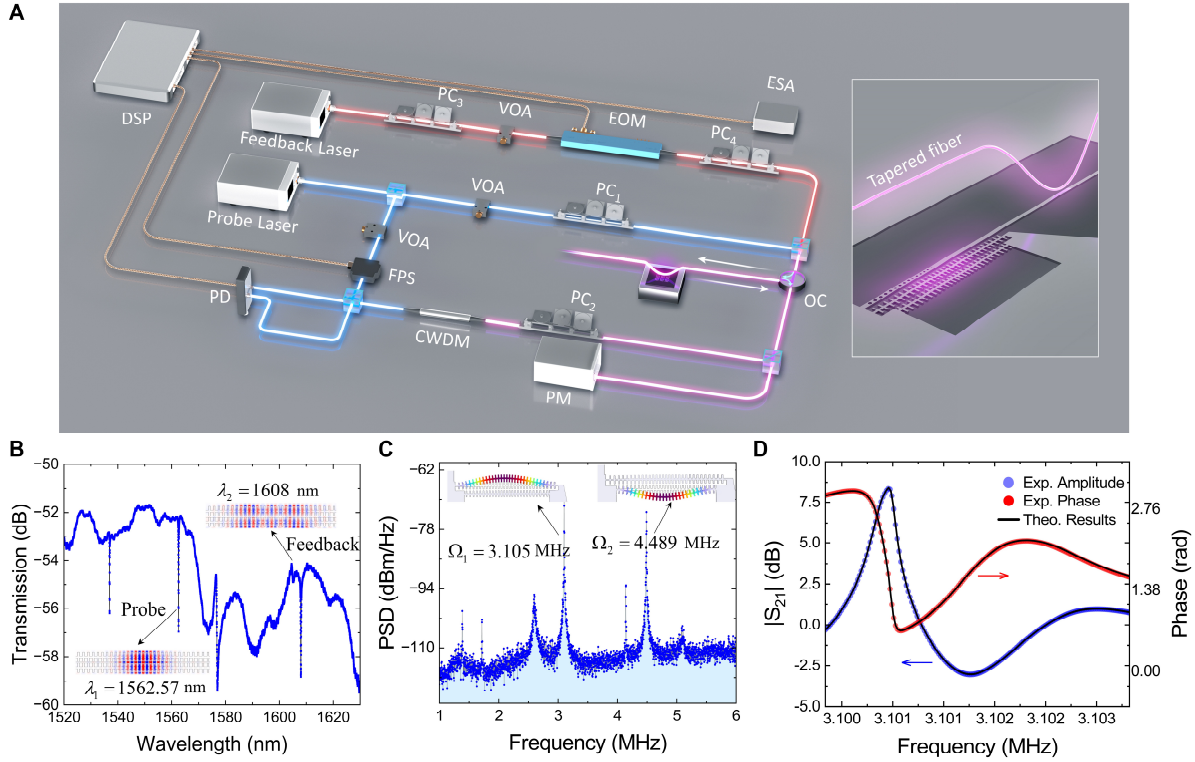


Fig. 2 Experimental setup and basic characterizations enabling higher-order EPs. (A) Schematic of the experimental setup. PC: polarization controller; VOA: variable optical attenuator; EOM: electro-optic modulator; OC: optical circulator; PM: power meter; CWDM: coarse wavelength-division multiplexer; FPS: fiber phase shifter; PD: photodetector; ESA: electrical spectrum analyzer; DSP: digital signal processor. (B) Optical reflection spectrum. The cavity modes near 1563 nm and 1608 nm are used to detect the displacement of the nanomechanical resonator and to realize feedback of virtual resonators, respectively. (C) Displacement power spectral density (PSD) of the mechanical motion in the MHz range. (D) S_{21} curve of the FPGA-based virtual-resonator module used to realize NEP₇.

To demonstrate the arbitrary-order LEPs and NEPs proposed above, we designed and fabricated a silicon optomechanical fishbone cavity (section S3). Fig. 1D shows the scanning electron microscope (SEM) image of the designed structure. The red area in Fig. 1D represents a fishbone nanobeam cavity that serves as the physical nanomechanical resonator for realizing EPs. Moreover, the periodic refractive index modulation near the boundary of the nanobeams localizes the optical field in the center of the defect region. The purple region is a reflective waveguide that couples light in and out through a tapered fiber attached above (Fig. 2A inset). The probe-feedback experimental setup was built to further demonstrate higher-order EPs (section S4), as shown in Fig. 2A. The probe laser was used to excite one optical cavity mode to read out the displacement

signal of the nanomechanical resonator via optomechanical interaction. Subsequently, the displacement signal was sent into the virtual resonators implemented on the FPGA-based digital signal processor (DSP). The computational feedback of the virtual-resonator module modulates the feedback laser that excites another optical mode, driving the mechanical mode via radiation pressure modulation.

Next, we present the basic characterization of the experimental system. The optical reflection spectrum is shown in Fig. 2B. The optical mode near 1563 nm with the fitted quality factor $Q_1 \approx 9977$ is driven by the probe laser, which is tuned to cavity resonance. The optical mode near 1608 nm with the fitted quality factor $Q_2 \approx 6030$ is driven by the pump laser, whose wavelength is detuned by 1.5 nm from the cavity resonant wavelength, to minimize the amplitude-dependent saturation of the optical spring effect (2, 33). Meanwhile, the mechanical spectrum acquired from balanced homodyne detection (40) is shown in Fig. 2C. The peaks at 3.105 MHz and 4.489 MHz correspond to the fundamental modes of the cavity's two nanobeams. In this study, we focus on the mechanical mode with frequency $\Omega_0/2\pi \approx 3.105$ MHz and quality factor $Q_m \approx 2512$ for realizing higher-order EPs. Its optomechanical coupling rates to the probe and feedback optical modes are estimated as $g_1/2\pi = 0.912$ MHz and $g_2/2\pi = 1.1514$ MHz, respectively. The response of the DSP-constructed virtual-resonator module is also characterized, as shown in Fig. 2D. The measured S_{21} curve of this module realizing NEP₇ reproduces the theoretical response. The feedback path delay t_0 introduces a phase φ_d in the coupling strength as $J_j e^{i(\varphi_j + \varphi_d)/2}$ ($j=1, \dots, n$). Here, $\varphi_d \approx (\Omega_m t_0 \bmod 2\pi)$ and serves as an additional tuning parameter controlling the distance from the EPs ($\varphi_d = 0$).

With this setup, higher-order EPs are demonstrated in Fig. 3. For simplicity, we begin by presenting the LEPs in Fig. 3A (section S10). We construct the LEPs with both parity-time symmetry and anti-parity-time symmetry to show the flexibility of this proposal. In the parity-time symmetry configuration, the second- and third-order LEPs (LEP₂ and LEP₃) are illustrated by tuning the coherent coupling strength (33). While the spectra near LEP₂ exhibit a square-root response, those near LEP₃ manifest a linear response as the system symmetry cancels the third-order response (17). The second-order EP with anti-parity-time symmetry is also realized by tuning the dissipative coupling strength (33) between two mechanical modes with distinct frequencies.

To access the phonon lasing regime and demonstrate NEPs, we reconfigure the FPGA by increasing the feedback gain and resetting the coefficients of virtual resonators, including the complex frequencies $\Omega_j - i\gamma_j/2$ and the coupling strengths $J_j^{NEP} e^{i\varphi_j/2}$. Fig. 3B shows the evolution of phonon lasing frequencies near NEP₃ as functions of the delay phase φ_d and the frequency shift Δf of the nanomechanical resonator. In contrast to the LEP case, only a single phonon lasing mode emerges near NEPs. The experimental data fall on the theoretical surface, which originates from a branch of the Riemann surface.

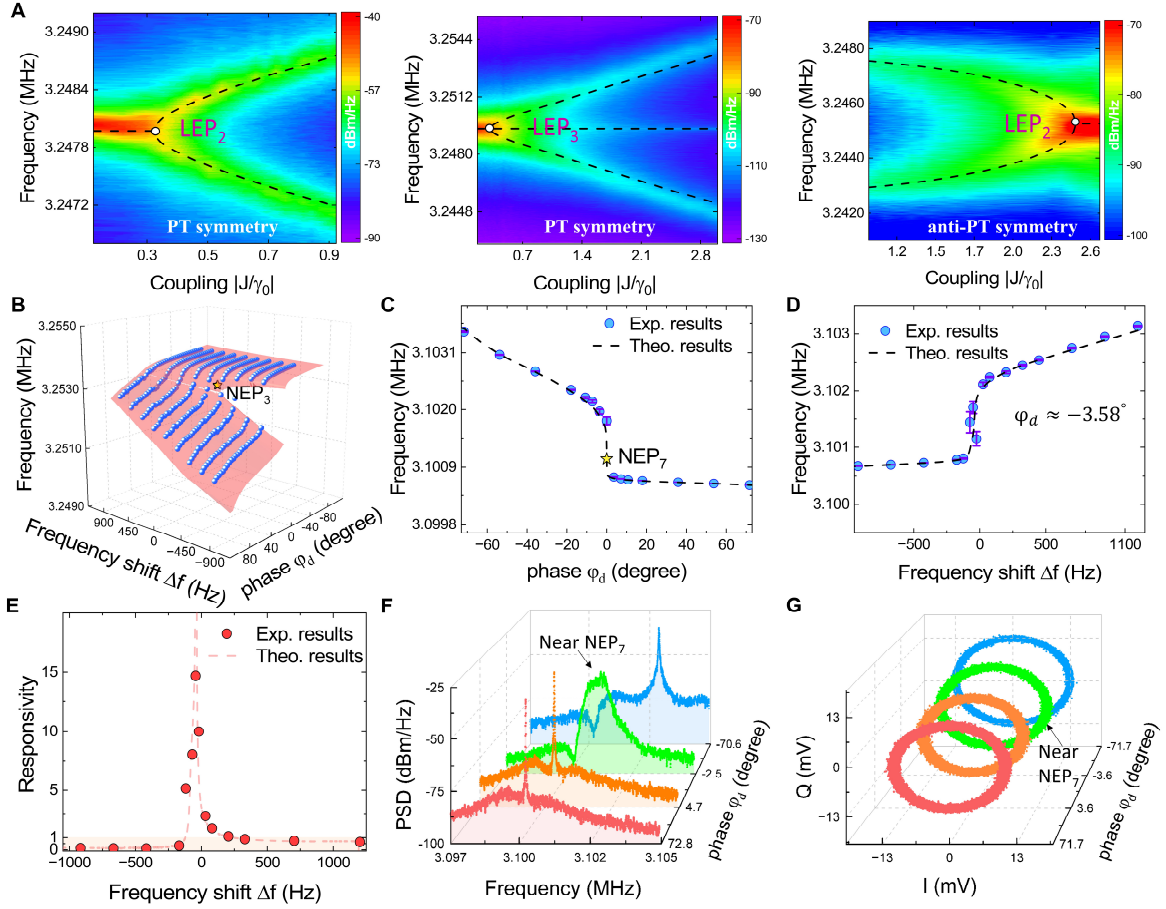


Fig. 3 Experimental demonstration of higher-order EPs. (A) Measured mechanical displacement PSD near LEPs, including PT-symmetric LEP₂/LEP₃ and anti-PT-symmetric LEP₂. (B) Lasing frequency evolution near NEP₃ as a function of the nanomechanical frequency shift Δf and the delay phase φ_d . (C) Mechanical lasing frequency versus φ_d near NEP₇. (D, E) Mechanical lasing frequencies (D) and the corresponding responsivities (E) versus Δf at $\varphi_d \approx -3.58^\circ$. In (E), the responsivities are derived by numerically differentiating the experimental lasing frequencies, with the nanomechanical resonator replaced by a virtual counterpart to improve accuracy. (F, G) Mechanical spectra near NEP₇ (F) and their complex amplitude representation (G) are shown

at multiple φ_d . Dashed lines in (A) and surface in (B) represent theoretical results; colormap in (A) and dots in (B) show experimental data. (B, D) The lasing frequency versus Δf is obtained by uniformly shifting all virtual-resonator frequencies Ω_j . (C, D) The error bars denote the Allan deviation at $\tau=0.1$ s and are doubled for clarity.

To further demonstrate the scalability and generality of this method, the evolution of lasing frequencies near NEP_7 is characterized in Fig. 3C–D following the same procedure as for the NEP_3 case. In Fig. 3C, the phase is tuned to $\varphi_d \approx 0$ to realize the NEP_7 . Subsequently, the evolution of the lasing frequencies with the nanomechanical frequency shift Δf is shown in Fig. 3D. The phase φ_d is adjusted to -3.58° to avoid the bistability region (41) for further noise analysis. This slight inconsistency between theoretical and experimental results in Fig. 3C–D arises from the drift of the nanomechanical resonant frequency (42) (section S9). Consequently, the responsivity $\partial\omega_{\text{las}}/\partial\varepsilon$, defined as the derivative of lasing frequency versus perturbation ε , cannot be determined accurately from Fig. 3D due to the frequency-drift-induced errors. To address this, we replace this real nanomechanical resonator with a virtual one that is highly stable, and perform numerical differentiation of experimental lasing frequencies to approximate $\partial\omega_{\text{las}}/\partial\varepsilon$ (section S9). The resulting responsivity is shown in Fig. 3E and greatly exceeds unity near NEP_7 . In contrast, Fig. 3F presents the mechanical spectra under the same conditions as in Fig. 3C and reveals a broader laser linewidth near NEP_7 . As shown in Fig. 3G, the in-phase/quadrature (I - Q) mechanical trajectory acquired over 10 s forms a limit cycle near NEP_7 , confirming that the nanobeam is in the phonon-lasing state and ruling out subthreshold amplification as the source of linewidth broadening. In fact, we attribute the observed linewidth broadening to the thermal and vacuum noise acting on the nanomechanical resonator. This interpretation is supported by the Allan deviation analysis in the following section and by the enhanced locking range observed near NEPs in the injection-locking experiment (section S6).

Further quantitative analysis of the noise is presented in Fig. 4 to investigate the fundamental sensitivity near NEPs. Specifically, Fig. 4A shows the Allan deviation $\sigma(\tau)$ (30) derived from the Fig. 3D datasets. The increased Allan deviation near NEP_7 corresponds to the linewidth broadening. Moreover, we find that the Allan deviation is measurement-port-dependent. The Allan deviation calculated from the measurement signal at the b_0 port, denoted as $\langle e_0 | \Psi_R \rangle$, deviates from the $-1/2$ slope expected at short averaging times τ on a log-log plot. If only the lasing mode is considered, the relative phase between the resonators will be constant, resulting in synchronization. Under this

condition, the noise will be independent of the measurement port. Therefore, the observed port-dependent noise originates from the other modes below the lasing threshold. By filtering out other modes using the projection $\langle \Psi_L^{las} | \Psi_R \rangle$, where Ψ_L^{las} is the estimated left eigenvector of the lasing mode, the Allan deviation follows the $-1/2$ slope for short τ (section S5).

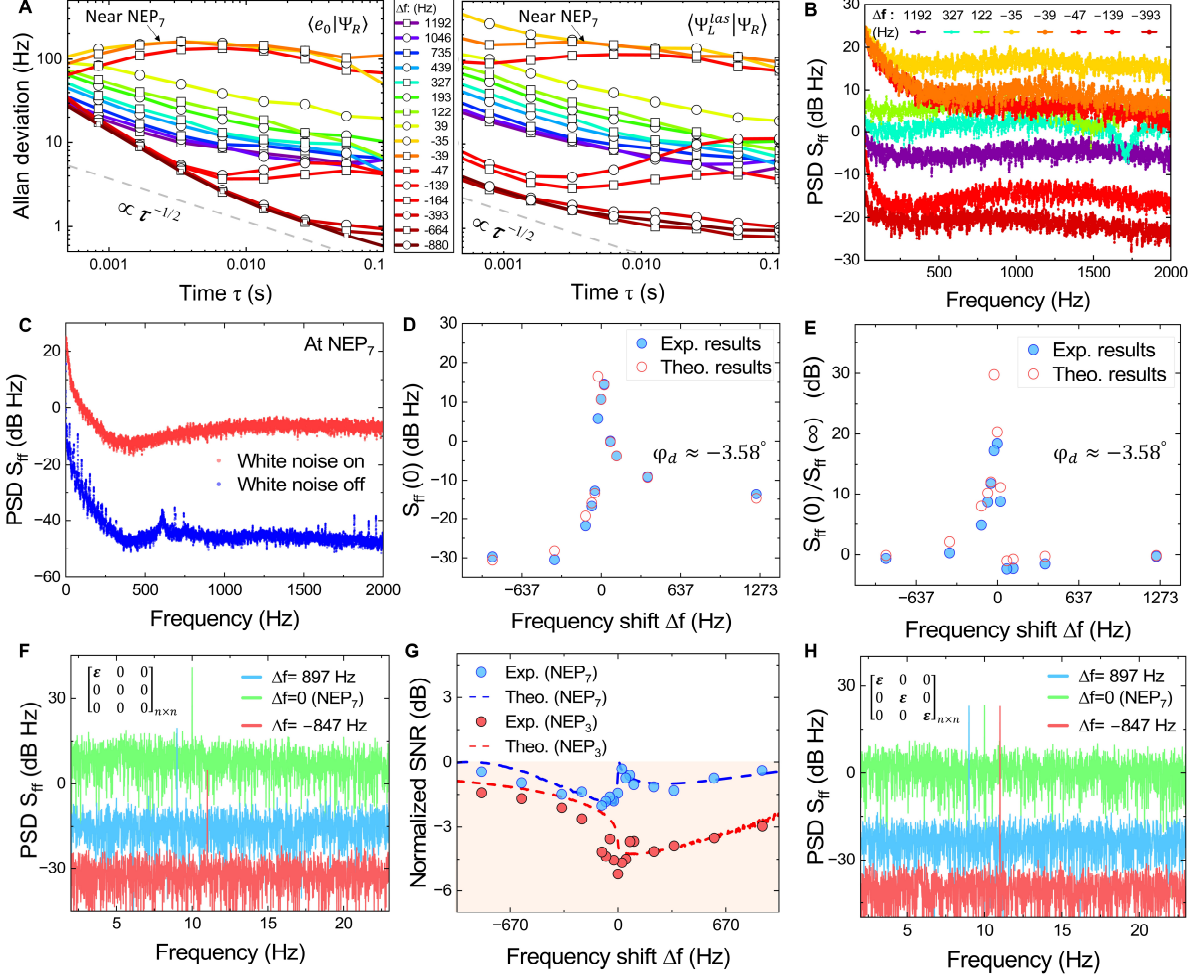


Fig. 4 Sensitivity analysis of higher-order NEPs. (A) Allan deviation under different projection bases. (B) PSD S_{ff} of measured instantaneous mechanical lasing frequency near NEP_7 , under the projection $\langle \Psi_L^{las} | \Psi_R \rangle$. (C) PSD S_{ff} at NEP_7 with and without additional white noise injected into port b_{in}^0 . (D, E) Evolution of the PSD S_{ff} versus the frequency shift Δf of mode b_0 near NEP_7 at $\varphi_d \approx -3.58^\circ$, displaying $S_{ff}(0)$ at 0 Hz (D) and the relative value $S_{ff}(0)/S_{ff}(\infty)$ (E). (F, H) PSD near NEP_7 at $\varphi_d = 0^\circ$ after applying a 10 Hz perturbation ε to the frequency of b_0 (F) and to all resonators (H). Spectra are horizontally offset for clarity. (G) Normalized SNR near higher-order NEPs at $\varphi_d = 0^\circ$. The orange region indicates that the SNR is lower than that of a single-mode phonon laser with the same phonon energy in b_0 . In (C-H), the nanomechanical resonator is replaced by a virtual resonator for noise analysis, excluding the influence of environmental parameter drift.

The corresponding PSD S_{ff} of the measured instantaneous lasing frequencies further illustrates this noise behavior (Fig. 4B). For high-frequency components, the frequency-jitter PSDs remain nearly flat, corresponding to the $-1/2$ slope of the Allan deviation. For low-frequency jitter, the PSDs lie above their high-frequency counterparts, especially near NEP₇. On the surface, this behavior might suggest that the long-term frequency drift (42), when treated as a signal, is more strongly amplified at low frequencies than thermal noise, thereby implying a fundamental sensitivity enhancement near NEPs. A similar conclusion can be drawn by comparing the high-frequency noise floor in S_{ff} with the responsivity (section S7). Nevertheless, we find that thermal noise can also lead to a frequency-dependent floor in S_{ff} , indicating that high-frequency jitter alone is insufficient to represent the fundamental noise. This unexpected finding raises a question of whether the fundamental sensitivity is truly enhanced near NEPs and how it scales with EP order.

We first verify the thermal-noise-induced frequency dependence of S_{ff} in Fig. 4C, where we replace the nanomechanical resonator with a virtual resonator to eliminate the frequency drift. Here, S_{ff} increases dramatically when additional electrical white noise, serving as an equivalent thermal-noise source, is injected through the b_0 port. This indicates that white noise becomes the dominant noise source. Counterintuitively, the equivalent thermal noise leads to a frequency-dependent noise floor in S_{ff} at NEP₇. Specifically, the actual frequency jitter at low frequencies is significantly larger than that at high frequencies, which is not captured by the traditional Petermann factor (27). This frequency-dependent jitter is further verified by Simulink simulations (section S8) and can be explained by the frequency-dependent feedback response.

$$\frac{d\hat{b}_0}{dt} = (-i\Omega_0 - \gamma_0/2)\hat{b}_0 + \sum_{j=1}^n J_j^{NEP} \sqrt{\zeta} e^{i\varphi_j/2} \hat{b}_j + \sqrt{\gamma_0} \hat{b}_m^0 \quad (1)$$

To further reveal the fundamental sensitivity of the NEP-based sensors, we analyze the Langevin equation for the mechanical mode b_0 , given by Eq. 1. Here, $J_j^{NEP} \sqrt{\zeta} e^{i\varphi_j/2}$ denotes the coupling strength between b_0 and the virtual mode b_j , while $\sqrt{\gamma_0} \hat{b}_m^0$ denotes the input noise drive from the thermal and vacuum fluctuations. For the high-frequency components of $\sqrt{\gamma_0} \hat{b}_m^0$, the relative feedback strength ζ cannot track these components, as their frequencies exceed the response bandwidth. In contrast, ζ can adiabatically follow the low-frequency noise perturbations, making the measured S_{ff} frequency-dependent. In the phonon lasing regime, the complex

amplitude of mode b_0 takes the form $B(t)e^{-i\phi(t)}$. Therefore, the drive $\sqrt{\gamma_0}b_{in}^0$ is given by $(\sqrt{\gamma_0}b_{in}^0 e^{i\phi(t)} / B(t))b_0(t) \approx \sqrt{\gamma_0/2}((X+iY)/\langle B(t) \rangle)b_0(t)$. This noise drive is equivalent to the fluctuation of the mechanical resonant frequency as $\sqrt{\gamma_0/2}Y/\langle B(t) \rangle$ and mechanical dissipation rate as $\sqrt{2\gamma_0}X/\langle B(t) \rangle$, where X and Y are independent white-noise processes. As a result, the perturbation ε to be measured, such as a shift in the mechanical frequency or linewidth, is mixed with the equivalent complex frequency jitter. The signal and noise therefore share the same system coupling channel and are amplified simultaneously within the system's feedback response bandwidth, implying that the fundamental sensitivity is not enhanced near NEPs of any order. For completeness, the fundamental sensitivity of LEPs is discussed in section S5 of the Supplementary Materials, where we reach a similar conclusion.

The above conclusion is first verified experimentally by estimating the PSD S_{ff} at 0 Hz in Fig. 4D and the relative PSD $S_{ff}(0)/S_{ff}(\infty)$ in Fig. 4E. These experimental results near NEP₇ are captured by the model that treats noise as equivalent parameter fluctuations (section S5). We further measure the SNR to examine whether NEPs provide any fundamental sensitivity enhancement. A 10 Hz perturbation ε is applied to the frequency of mode b_0 (section S8), and the frequency shift Δf of b_0 is swept across NEP₇ ($\varphi_d = 0$). As expected, the resulting PSD in Fig. 4F exhibits a peak at 10 Hz, well above the frequency-noise floor. However, no evidence of sensitivity enhancement near NEP₇ is observed. Furthermore, the measured SNRs near NEP₃ and NEP₇, normalized to the SNR of a single-mode laser with the same energy in b_0 , are shown in Fig. 4G. These experimental results are in good agreement with the theoretical formula (section S5). Contrary to the prevailing expectation, the normalized SNR is below unity, indicating that the sensing performance of NEP-based sensors does not surpass that of a simple single-mode laser. Since the frequency fluctuations $\sqrt{2\gamma_0}Y/\langle B(t) \rangle$ alone would yield a normalized SNR of unity, the observed reduction in SNR stems from additional dissipation fluctuations $\sqrt{2\gamma_0}X/\langle B(t) \rangle$. The dissipation fluctuations generate redundant lasing frequency jitter, thereby making the enhancement of the signal smaller than that of the noise near NEPs. These results confirm that the higher-order NEPs do not provide fundamental sensitivity enhancement.

Although fundamental sensitivity enhancement is absent, the measured sensitivity can still be enhanced in the presence of additional technical noise (11, 12). Specifically, we apply a global frequency fluctuation equally to all the resonators. This perturbation changes only the real part of

the Hamiltonian's trace and does not affect the EP dynamics. As shown in Fig. 4H, this additional frequency fluctuation is not amplified near the NEP_7 . This kind of technical perturbation is common in real systems. For instance, temperature and humidity fluctuations affect all resonators identically, and the probe laser frequency jitter in Ref. (12) effectively acts as a perturbation to the real part of the Hamiltonian's trace near the LEP_2 . Consequently, higher-order EPs can still offer practical advantages for sensor applications in noisy environments through such non-fundamental sensitivity enhancement.

Discussion

In this study, we present a general architecture for realizing arbitrary-order EPs via a hybrid physical–digital recurrent network. With a single nanomechanical resonator, we experimentally demonstrate reconfigurable and scalable higher-order EPs in both linear and nonlinear regimes. Our approach addresses the intrinsic challenge posed by the topological fragility near higher-order EPs. It also obviates the need for both the resolved-sideband condition (21, 33) and mechanical-parameter-mismatch compensation (43, 44) when realizing EPs in optomechanical systems.

Furthermore, we investigate the sensitivity near EPs. Our analysis shows that the fundamental noise component and the signal enter the system through the same channel and are co-amplified. This mechanism indicates that the fundamental sensitivity is not enhanced near EPs regardless of their order, and this conclusion is supported by direct SNR measurements near NEP_3 and NEP_7 . Despite the lack of fundamental sensitivity enhancement, the EPs remain effective for improving sensitivity in technical-noise-dominant systems (11, 12). Consequently, higher-order EPs can be practically useful for detecting physical quantities such as acceleration (11), spin (45), displacement (12), and mass (46).

In summary, our study demonstrates a general platform for realizing higher-order EPs and clarifies the long-standing debate on fundamental sensitivity enhancement in non-Hermitian sensors. Beyond its current realization, this programmable architecture opens avenues for exploring high-dimensional non-Hermitian topology and developing distributed sensing protocols that leverage exceptional points, quantum optomechanics, and artificial intelligence.

References and Notes

1. G. Gamow, The quantum theory of nuclear disintegration. *Nature* **122**, 805–806 (1928).
2. M. Aspelmeyer, T. J. Kippenberg, F. Marquardt, Cavity optomechanics. *Rev. Mod. Phys.* **86**, 1391–1452 (2014).
3. M. Fruchart, R. Hanai, P. B. Littlewood, V. Vitelli, Non-reciprocal phase transitions. *Nature* **592**, 363–369 (2021).
4. J. P. Cavalcante, M. Richartz, B. C. Da Cunha, Exceptional point and hysteresis in perturbations of Kerr black holes. *Phys. Rev. Lett.* **133**, 261401 (2024).
5. Y.-W. Lu, W. Li, X.-H. Wang, Quantum and classical exceptional points at the nanoscale: properties and applications. *ACS Nano* **19**, 17953–17978 (2025).
6. A. Li, H. Wei, M. Cotrufo, W. Chen, S. Mann, X. Ni, B. Xu, J. Chen, J. Wang, S. Fan, C.-W. Qiu, A. Alù, L. Chen, Exceptional points and non-Hermitian photonics at the nanoscale. *Nat. Nanotechnol.* **18**, 706–720 (2023).
7. Ş. K. Özdemir, S. Rotter, F. Nori, L. Yang, Parity–time symmetry and exceptional points in photonics. *Nat. Mater.* **18**, 783–798 (2019).
8. M.-A. Miri, A. Alù, Exceptional points in optics and photonics. *Science* **363**, eaar7709 (2019).
9. R. El-Ganainy, K. G. Makris, M. Khajavikhan, Z. H. Musslimani, S. Rotter, D. N. Christodoulides, Non-Hermitian physics and PT symmetry. *Nat. Phys.* **14**, 11–19 (2018).
10. J.-H. Park, A. Ndao, W. Cai, L. Hsu, A. Kodigala, T. Lepetit, Y.-H. Lo, B. Kanté, Symmetry-breaking-induced plasmonic exceptional points and nanoscale sensing. *Nat. Phys.* **16**, 462–468 (2020).
11. R. Kononchuk, J. Cai, F. Ellis, R. Thevamaran, T. Kottos, Exceptional-point-based accelerometers with enhanced signal-to-noise ratio. *Nature* **607**, 697–702 (2022).
12. J. Xu, Y. Mao, Z. Li, Y. Zuo, J. Zhang, B. Yang, W. Xu, N. Liu, Z. J. Deng, W. Chen, K. Xia, C.-W. Qiu, Z. Zhu, H. Jing, K. Liu, Single-cavity loss-enabled nanometrology. *Nat. Nanotechnol.* **19**, 1472–1477 (2024).
13. P. Miao, Z. Zhang, J. Sun, W. Walasik, S. Longhi, N. M. Litchinitser, L. Feng, Orbital angular momentum microlaser. *Science* **353**, 464–467 (2016).
14. H. Xu, D. Mason, L. Jiang, J. G. E. Harris, Topological energy transfer in an optomechanical system with exceptional points. *Nature* **537**, 80–83 (2016).

15. A. Schumer, Y. G. N. Liu, J. Leshin, L. Ding, Y. Alahmadi, A. U. Hassan, H. Nasari, S. Rotter, D. N. Christodoulides, P. LiKamWa, M. Khajavikhan, Topological modes in a laser cavity through exceptional state transfer. *Science* **375**, 884–888 (2022).
16. Q. Song, M. Odeh, J. Zúñiga-Pérez, B. Kanté, P. Genevet, Plasmonic topological metasurface by encircling an exceptional point. *Science* **373**, 1133–1137 (2021).
17. H. Hodaiei, A. U. Hassan, S. Wittek, H. Garcia-Gracia, R. El-Ganainy, D. N. Christodoulides, M. Khajavikhan, Enhanced sensitivity at higher-order exceptional points. *Nature* **548**, 187–191 (2017).
18. Q. Zhong, J. Kou, Ş. K. Özdemir, R. El-Ganainy, Hierarchical Construction of Higher-Order Exceptional Points. *Phys. Rev. Lett.* **125**, 203602 (2020).
19. X. Zhou, X. Ren, D. Xiao, J. Zhang, R. Huang, Z. Li, X. Sun, X. Wu, C.-W. Qiu, F. Nori, H. Jing, Higher-order singularities in phase-tracked electromechanical oscillators. *Nat. Commun.* **14**, 7944 (2023).
20. I. Mandal, E. J. Bergholtz, Symmetry and Higher-Order Exceptional Points. *Phys. Rev. Lett.* **127**, 186601 (2021).
21. Y. S. S. Patil, J. Höller, P. A. Henry, C. Guria, Y. Zhang, L. Jiang, N. Kralj, N. Read, J. G. E. Harris, Measuring the knot of non-Hermitian degeneracies and non-commuting braids. *Nature* **607**, 271–275 (2022).
22. Y. Wu, Y. Wang, X. Ye, W. Liu, Z. Niu, C.-K. Duan, Y. Wang, X. Rong, J. Du, Third-order exceptional line in a nitrogen-vacancy spin system. *Nat. Nanotechnol.* **19**, 160–165 (2024).
23. P.-R. Han, W. Ning, X.-J. Huang, R.-H. Zheng, S.-B. Yang, F. Wu, Z.-B. Yang, Q.-P. Su, C.-P. Yang, S.-B. Zheng, Measuring topological invariants for higher-order exceptional points in quantum three-mode systems. *Nat. Commun.* **15**, 10293 (2024).
24. K. Bai, T.-R. Liu, L. Fang, J.-Z. Li, C. Lin, D. Wan, M. Xiao, Observation of nonlinear exceptional points with a complete basis in dynamics. *Phys. Rev. Lett.* **132**, 073802 (2024).
25. H. Loughlin, V. Sudhir, Exceptional-point sensors offer no fundamental signal-to-noise ratio enhancement. *Phys. Rev. Lett.* **132**, 243601 (2024).
26. X. Zheng, Y. D. Chong, Noise constraints for nonlinear exceptional point sensing. *Phys. Rev. Lett.* **134**, 133801 (2025).
27. H. Wang, Y.-H. Lai, Z. Yuan, M.-G. Suh, K. Vahala, Petermann-factor sensitivity limit near an exceptional point in a Brillouin ring laser gyroscope. *Nat. Commun.* **11**, 1610 (2020).

28. A. Suntharalingam, L. Fernández-Alcázar, R. Kononchuk, T. Kottos, Noise resilient exceptional-point voltmeters enabled by oscillation quenching phenomena. *Nat. Commun.* **14**, 5515 (2023).
29. A. Roy, S. Jahani, Q. Guo, A. Dutt, S. Fan, M.-A. Miri, A. Marandi, Nondissipative non-Hermitian dynamics and exceptional points in coupled optical parametric oscillators. *Optica* **8**, 415–421 (2021).
30. Y.-H. Lai, Y.-K. Lu, M.-G. Suh, Z. Yuan, K. Vahala, Observation of the exceptional-point-enhanced Sagnac effect. *Nature* **576**, 65–69 (2019).
31. Y. Li, Y.-G. Peng, L. Han, M.-A. Miri, W. Li, M. Xiao, X.-F. Zhu, J. Zhao, A. Alù, S. Fan, C.-W. Qiu, Anti-parity-time symmetry in diffusive systems. *Science* **364**, 170–173 (2019).
32. A. Youssefi, S. Kono, A. Bancora, M. Chegnizadeh, J. Pan, T. Vovk, T. J. Kippenberg, Topological lattices realized in superconducting circuit optomechanics. *Nature* **612**, 666–672 (2022).
33. N. Wu, K. Cui, Q. Xu, X. Feng, F. Liu, W. Zhang, Y. Huang, On-chip mechanical exceptional points based on an optomechanical zipper cavity. *Sci. Adv.* **9**, eabp8892 (2023).
34. D. Mason, J. Chen, M. Rossi, Y. Tsaturyan, A. Schliesser, Continuous force and displacement measurement below the standard quantum limit. *Nat. Phys.* **15**, 745–749 (2019).
35. H. Yu, L. McCuller, M. Tse, N. Kijbunchoo, L. Barsotti, N. Mavalvala, et al., Quantum correlations between light and the kilogram-mass mirrors of LIGO. *Nature* **583**, 43–47 (2020).
36. W. P. Bowen, G. J. Milburn, *Quantum Optomechanics* (CRC Press, Boca Raton, FL, 2016).
37. G. Huang, A. Beccari, N. J. Engelsen, T. J. Kippenberg, Room-temperature quantum optomechanics using an ultralow noise cavity. *Nature* **626**, 512–516 (2024).
38. S. Assaworarith, X. Yu, S. Fan, Robust wireless power transfer using a nonlinear parity-time-symmetric circuit. *Nature* **546**, 387–390 (2017).
39. D.-Y. Chen, L. Dong, Q.-A. Huang, Inductor-capacitor passive wireless sensors using nonlinear parity-time symmetric configurations. *Nat. Commun.* **15**, 9312 (2024).
40. J. Guo, R. Norte, S. Gröblacher, Feedback cooling of a room temperature mechanical oscillator close to its motional ground state. *Phys. Rev. Lett.* **123**, 223602 (2019).
41. Z. Li, C. Li, G. Xu, W. Chen, Z. Xiong, H. Jing, J. S. Ho, C.-W. Qiu, Synergetic positivity of loss and noise in nonlinear non-Hermitian resonators. *Sci. Adv.* **9**, eadi0562 (2023).

42. M. Sansa, E. Sage, E. C. Bullard, M. Gély, T. Alava, E. Colinet, A. K. Naik, L. G. Villanueva, L. Duraffourg, M. L. Roukes, G. Jourdan, S. Hentz, Frequency fluctuations in silicon nanoresonators. *Nat. Nanotechnol.* **11**, 552–558 (2016).
43. H. Xu, L. Jiang, A. A. Clerk, J. G. E. Harris, Nonreciprocal control and cooling of phonon modes in an optomechanical system. *Nature* **568**, 65–69 (2019).
44. J. Del Pino, J. J. Slim, E. Verhagen, Non-Hermitian chiral phononics through optomechanically induced squeezing. *Nature* **606**, 82–87 (2022).
45. D. Rugar, R. Budakian, H. J. Mamin, B. W. Chui, Single spin detection by magnetic resonance force microscopy. *Nature* **430**, 329–332 (2004).
46. S. Dominguez-Medina, S. Fostner, M. Defoort, M. Sansa, A.-K. Stark, M. A. Halim, E. Vernhes, M. Gely, G. Jourdan, T. Alava, P. Boulanger, C. Masselon, S. Hentz, Neutral mass spectrometry of virus capsids above 100 megadaltons with nanomechanical resonators. *Science* **362**, 918–922 (2018).

Acknowledgments: The authors express their gratitude to Tianjin H-Chip Technology Group Corporation, Innovation Center of Advanced Optoelectronic Chip and Institute for Electronics and Information Technology in Tianjin, Tsinghua University for their fabrication support with electron beam lithography (EBL) and inductively coupled plasma (ICP) etching.

Funding:

National Key R&D Program of China (2023YFB2806703)

National Natural Science Foundation of China grant No. U22A6004

Beijing Frontier Science Center for Quantum Information

Beijing Academy of Quantum Information Sciences

Author contributions:

Conceptualization: NW

Methodology: NW

Investigation: NW, KC

Supervision: KC, YH

Writing – original draft: NW, KC

Writing – review & editing: NW, KC, ZC, CW, XF, FL, WZ, HS, YL, YH

Competing interests: Authors declare that they have no competing interests.

Data and materials availability: All data needed to evaluate the conclusions in the paper are present in the paper and the Supplementary Materials.